Available online at www.sciencedirect.com
ScienceDirect
Acta Materialia 56 (2008) 3914–3926
Acta MATERIALIA
www.elsevier.com/locate/actamat

Orientation image-based micromechanical modelling of subgrain texture evolution in polycrystalline copper

Ricardo A. Lebensohn [a,*], Renald Brenner [b], Olivier Castelnau [b], Anthony D. Rollett [c]

[a] Materials Science and Technology Division, Los Alamos National Laboratory, Los Alamos, NM 87544, USA
[b] Laboratoire des Proprietés Mécaniques et Thermodynamiques des Matériaux, Université Paris XIII, Av J.-B.Clement, 93430 Villetaneuse, France
[c] Department of Materials Science and Engineering, Carnegie-Mellon University, Pittsburgh, PA 15213, USA

Received 25 October 2007; received in revised form 9 April 2008; accepted 9 April 2008
Available online 12 May 2008

Abstract

An efficient full-field formulation based on fast Fourier transforms (FFTs) for the prediction of the viscoplastic deformation of polycrystals is applied to the study of the subgrain texture and microstructure evolution in polycrystalline Cu deformed under tension. Direct input from orientation imaging microscopy (OIM) images is used in the construction of the initial unit cell. Average orientations and misorientations predicted after 11% tensile strain are directly compared with OIM measurements, showing good agreement. The differences between misorientations of surface grains compared with bulk grains are estimated, and the orientation dependence of intragranular misorientations is studied. Measurements and simulations agree in that grains with initial orientation near $\langle 1\,1\,0\rangle$ tend to develop higher misorientations. This behavior can be explained in terms of attraction towards the two stable orientations and grain interaction. Only models that account explicitly for interaction between individual grains, like the FFT-based formulation, are able to capture these effects.
Published by Elsevier Ltd on behalf of Acta Materialia Inc.

Keywords: Texture; Microstructure; Copper; Orientation imaging microscopy; Micromechanical modelling

1. Introduction

The prediction of the mechanical behavior of plastically deforming polycrystalline materials, based on the directional properties and evolving microstructure of their constituent single-crystal grains is a nowadays a central problem in computational materials science. In recent years, the advances in the theories that link microstructures and properties of nonlinear heterogeneous materials have enabled the development of new concepts and algorithms for the prediction of the effective plastic response of statistically defined classes of polycrystalline aggregates using mean-field approaches (e.g. [1–3]), and also of the actual micromechanical fields that develop inside the grains of a given polycrystal with a particular microstructure.

The finite element method (FEM) has been extensively applied to solve the latter problem, with the aim of obtaining full-field solutions for the plastic deformation of polycrystalline materials, with intracrystalline resolution (e.g. [4–17]). However, the difficulties related to meshing and the large number of degrees of freedom required by such FEM calculations may limit the complexity and the size of the microstructures that can be investigated by these methods. While some of the above FEM calculations used "synthetic" three-dimensional (3D) microstructures, generated with space-filling regular [6,12,15] or Voronoi [8,9,14] polyhedra, other approaches [4,5,7,10,11,13,16] used electron back-scattering diffraction (EBSD)-based orientation imaging microscopy (OIM) experimental data on local orientations and grain morphology of face-centered cubic (fcc) polycrystals as input to the simulations. In most of

* Corresponding author.
E-mail address: lebenso@lanl.gov (R.A. Lebensohn).

1359-6454/$34.00 Published by Elsevier Ltd on behalf of Acta Materialia Inc.
doi:10.1016/j.actamat.2008.04.016

the latter approaches the orientation data was collected from the free 2D surface of a Cu or Al specimen. In some cases, the use of 2D data was fully justified, owing to the 2D multicrystal character of the measured specimen [7,10,11,14]. In other cases, the actual 3D microstructure beneath the measured 2D orientation maps was disregarded [4,5]. Recently, Musienko et al. [16] used OIM in combination with an etching technique to obtain the actual 3D grain structure of the near-surface region of a polycrystalline Cu specimen. The obvious limitation of this destructive technique is that only the post-deformation 3D structure can be reconstructed. However, the differences with the undeformed structure should not be large at moderate strains.

The typical output of these FEM calculations consisted of the effective stress–strain response and the local mechanical fields, along with overall and local textures. Several of the above FEM analyses also used post-deformation OIM data for comparison and validation of the corresponding predictions of intragranular orientation dispersions [5,7,11–13,16]. However, these comparisons were qualitative (e.g. in terms of "clouds" of poles representing orientations of material points belonging to a given grain). The development of a methodology for a quantitative comparison of local orientation data and corresponding predictions is one of the objectives of this work.

Besides the aforementioned efforts to link orientation measurements, microstructure evolution and FEM simulations, different experimental techniques have been applied to the characterization of orientation-dependent microstructures and local mechanical behavior. While transmission electron microscopy (TEM) has been the tool of choice for direct observation at sub-micron resolution of dislocation structures (and their orientations in three dimensions) inside crystals of fcc aggregates, and for studying their dependence on the grain's (final) orientation (e.g. [17,18]), OIM techniques have been applied to obtain 2D maps of intragranular orientation heterogeneity (with resolutions typically limited to the order of 1 μm) in bulk grains after deformation (e.g. [19,20] in Al), and also to follow the evolution of local orientations of surface grains with deformation (e.g. [21] in Cu). Concerning the measurement of such local orientation evolution in bulk grains, it is worth mentioning the pioneering work of Panchanadeeswaran et al. [22] who analyzed the channel-die compression of Al using OIM and a split sample technique. There has also been a recent 3D X-ray diffraction (3DXRD) characterization of the lattice rotations and orientation spread of individual bulk grains of a polycrystalline Al sample deformed in tension [23,24]. In what follows, when appropriate, some of the above results will be compared qualitatively with our own measurements and predictions.

The determination of the mean orientation inside constituent grains, and the distribution of misorientations with respect to this average orientation, is nowadays a standard procedure to provide a quantitative measure of the orientation heterogeneity in a polycrystalline sample. The quaternion representation of crystallographic orientations [25] is a very useful tool to compute these statistical quantities [26–29]. The use of 2D orientation maps for the determination of ensembles of pixels representing sections of grains, along with the calculation of mean orientations (averaging with equal weight the orientation of every pixel belonging to a given grain) and the corresponding average misorientations (averaging the misorientation of every pixel with respect to the mean orientation), are standard built-in features of commercial OIM software. The misorientation distribution of a given grain, however, is generally anisotropic in orientation space. Therefore, besides the average misorientation (i.e. the first-order moment of the distribution), higher-order moments [20] should be used for a more accurate characterization of such distribution. In this work, however, the misorientation analysis will be restricted to the first-order moment of the distributions, for the sake of simplicity.

Conceived as a very efficient alternative to micromechanical FEM methods (whose calculation times usually scale with N^2, where N is the number of discretization points), a formulation inspired by image-processing techniques and based on the fast Fourier transform (FFT) algorithm (which is a $N \times \log N$ algorithm) has been recently proposed to predict the micromechanical behavior of plastically deforming heterogeneous materials. The latter includes both composites [30–32], in which the source of heterogeneity is related to the spatial distribution of phases with different mechanical properties, and polycrystals [2,33–35], in which the heterogeneity is related to the spatial distribution of crystals with directional mechanical properties. Owing to its image-processing lineage, this formulation is particularly suitable for use with direct input from actual images of the material, e.g. optical or scanning electron microscopy (SEM) images that show the phase distribution in the case of composites [30], or orientation images in the case of polycrystals. The latter will be used here for a quantitative study of the average orientations and intragranular misorientations developed in a Cu polycrystal deformed in tension.

The plan of the paper is as follows. In Section 2, we describe the recollection and processing techniques of the OIM images subsequently used for input and validation of our orientation image-based modeling of the subgrain texture evolution of a Cu aggregate deformed 11% in tension. In Section 3, we present in detail the FFT-based formulation, specialized to viscoplastic polycrystals. In Section 4, we describe the construction of a 3D unit cell, based on the OIM image of the undeformed Cu sample. In Section 5, we compare experimental data on the reorientation of individual grains and the development of intragranular misorientations with corresponding simulations, with emphasis on the correlation between these measures/simulations and the orientations of the grains. Lastly, the advantages and limitations of the proposed methodology are discussed in Section 6, as well as some possible improvements.

2. Experimental

EBSD-based OIM was used to characterize the local orientations measured in an area of about 500×500 μm, located on one of the flat surfaces of a recrystallized Cu sample. The spatial resolution (given by the distance between two consecutive pixels) was 2 μm in each direction. Two OIM images were taken, one from the undeformed sample, and another after 11% tensile strain along the y-direction (deformation was carried out at room temperature). The scanned area of the deformed sample (332×445 pixels) was larger than that of the initial microstructure (274×339 pixels), and contained more orientations (2429 vs. 1585 grains). This allowed us to register the images, and thus to identify the ID numbers given by the OIM software to each individual grain (which are in general different from one image to the other), before and after deformation. The registration was carried out by: (a) identifying, by visual inspection of areas and shapes (which were little affected by 11% strain), to obtain the IDs of the five grains with the largest area in both images, and (b) optimizing the relative position of the initial (smaller) image inside the final (larger) image. For a given relative position of both images, every pair of overlapping pixels was analyzed. Each time the corresponding IDs of each of the five largest grains in both images coincided, the "score" of the comparison was improved, while every disagreement was penalized. Once the two images were appropriately registered, a correlation table (based essentially on the determination of the pixel partition of every grain belonging to one image among the grains of the other image) allowed us to identify the ID numbers of 57 of the grains with largest areas, in the pre- and post-deformation images, for further comparisons. We note that besides considering the number of pixels belonging to each grain as a 2D measure of its apparent size (with the obvious limitation of underestimating the size of grains located close to the image's edges), the square root of this number will be also used as a 1D measure (i.e. in units of length) of the apparent grain size.

The OIM software gives the average orientation and the average intragranular misorientation of every identified grain. The former is defined as the orientation that, on average, has the minimum misorientation with respect to the orientation of every pixel belonging to the grain. Both quantities can be readily calculated using quaternion algebra (see Ref. [29] for details). The initial per-grain average misorientation distribution is shown in Fig. 1a (mean value $= 0.71°$, max value $= 2.86°$). After 11% strain, the mean value over the 2429 orientations of the per-grain average misorientation reached 1.71°, with a maximum value of 6.62° and a distribution shown in Fig. 1b. The comparison of the latter with the misorientation distribution of the undeformed state clearly indicates that the average intragranular misorientations measured after 11% strain were essentially due to the plastic deformation. It is worth noting that the accuracy of the average values of

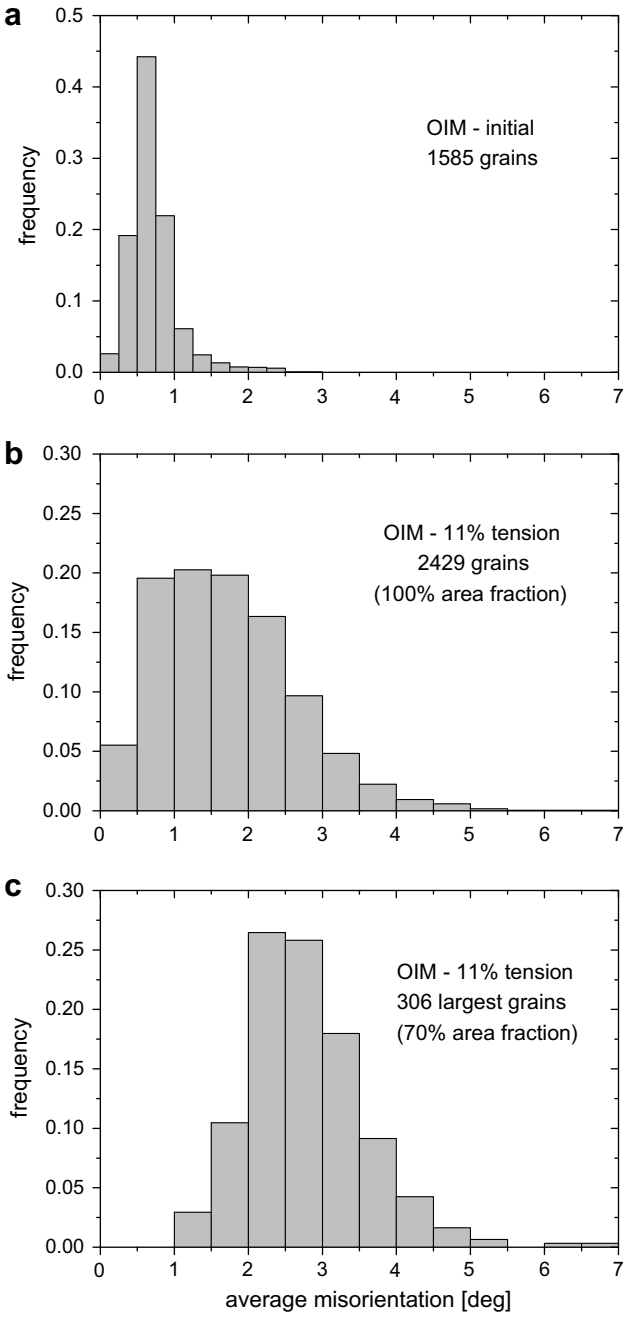

Fig. 1. Average intragranular misorientations, extracted from the scanned area of the deformed Cu sample: (a) initial distribution; (b) after 11% tension: full distribution, accounting for 2429 grains; (c) after 11% tension: distribution corresponding to the 306 largest grains of the image, representing 70% of the area fraction.

orientation and misorientation in the grains delivered by the OIM software was confirmed by our own quaternion-based analysis, developed for the post-processing of the FFT-based results (see below).

The individual counts of the histogram of Fig. 1b corresponds to the entire scanned area, in which the grains exhibit a wide range of area sizes (number of pixels), with almost one-half corresponding to domains with less than 10 pixels. In contrast, Fig. 1c shows the average misorien-

tation distribution for the 306 largest grains (with more than 100 pixels each) representing 70% of the image's area fraction. The mean value of the latter distribution is noticeably higher (2.78°) than the one corresponding to grains of all area sizes. This suggests that larger grains tend to develop larger misorientations (in agreement with Pantleon et al. [20] observations in cold-rolled Al), or that counting average misorientations of very small grains (hence, using too few sampling points for computation) produces a bias of the distribution towards smaller values. To elucidate this question, Fig. 2 shows the average misorientation of individual grains as a function of their area size (in pixels). While smaller grains exhibit both small and large misorientations, likely correlated with their particular orientation and neighborhood (as also reported in Ref. [20]), most of the larger grains show above average misorientations. Also, excluding very small grains in which the statistics is poor, it is apparent that larger grains tend to develop higher average misorientations.

3. Model

The FFT-based full-field formulation for viscoplastic polycrystals is conceived for periodic unit cells, provides an exact solution of the governing equations, and has better numerical performance than a FE calculation for the same purpose and resolution. It was originally developed [30,31] as a fast algorithm to compute the elastic and elastoplastic effective and local response of composites, and later adapted [2,33–35] to deal with the viscoplastic deformation of 3D power-law polycrystals. It shares some common characteristics with the phase field method, although it is limited to what in phase field jargon is known as long-range interactions (e.g. [36]), since no heterogeneous chemical energy term is involved in the mechanical response and/or microstructure evolution of a single-phase polycrystal. Recently, a similar kind of phase field analysis

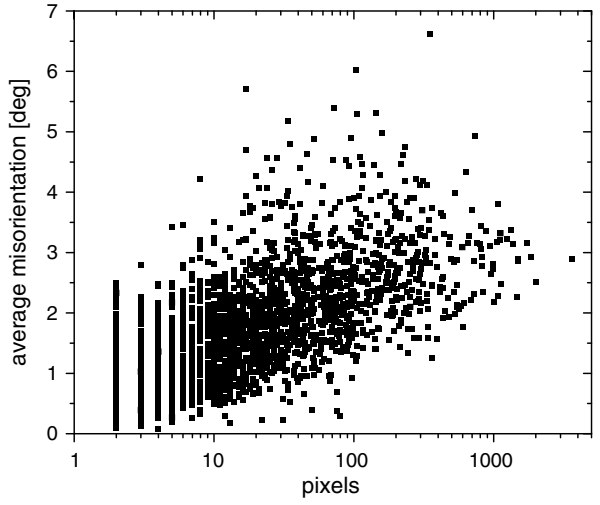

Fig. 2. Average intragranular misorientations after 11% tensile deformation of the entire set of 2429 grains, as a function of grain size (in pixels).

was proposed [37] to obtain the local fields in elastically heterogeneous polycrystals. The FFT-based approach, however, is not restricted to linear behaviors. Problems involving non-linear materials (e.g. viscoplastic polycrystals) are treated similarly to a linear problem, using the concept of linear reference material [30,31].

Briefly, the viscoplastic FFT-based formulation consists in finding a strain-rate field, associated with a kinematically admissible velocity field, that minimizes the average of local work-rate, under the compatibility and equilibrium constraints. The method is based on the fact that the local mechanical response of a heterogeneous medium can be calculated as a convolution integral between Green functions associated with appropriate fields of a linear reference homogeneous medium and the actual heterogeneity field. For periodic media, use can be made of the Fourier transform to reduce convolution integrals in real space to simple products in Fourier space. Thus, the FFT algorithm can be utilized to transform the heterogeneity field into Fourier space and, in turn, to get the mechanical fields by transforming that product back to real space. However, the actual heterogeneity field depends precisely on the a priori unknown mechanical fields. Therefore, an iterative scheme has to be implemented to obtain, upon convergence, a compatible strain-rate field and a stress field in equilibrium.

A periodic unit cell representing the polycrystal is discretized into $N_1 \times N_2 \times N_3$ Fourier points. This discretization determines a regular grid in the Cartesian space $\{\mathbf{x}^{\mathbf{d}}\}$ and a corresponding grid in Fourier space $\{\boldsymbol{\xi}^{\mathbf{d}}\}$. Velocities and tractions along the boundary of the unit cell are left undetermined. An average velocity gradient $V_{i,j}$ is imposed to the unit cell, which can be decomposed into an average strain-rate $\dot{E}_{ij} = \frac{1}{2}(V_{i,j} + V_{j,i})$ and average rotation-rate $\dot{\Omega}_{ij} = \frac{1}{2}(V_{i,j} - V_{j,i})$. The local strain-rate field is a function of the local velocity field, i.e. $\dot{\varepsilon}_{ij}(v_k(\mathbf{x}))$, and can be split into its average and a fluctuation term: $\dot{\varepsilon}_{ij}(v_k(\mathbf{x})) = \dot{E}_{ij} + \tilde{\dot{\varepsilon}}_{ij}(\tilde{v}_k(\mathbf{x}))$, where $v_i(\mathbf{x}) = \dot{E}_{ij}x_j + \tilde{v}_i(\mathbf{x})$. By imposing periodic boundary conditions, the velocity fluctuation field $\tilde{v}_k(\mathbf{x})$ is assumed to be periodic across the boundary of the unit cell, while the traction field is antiperiodic, to meet equilibrium on the boundary between contiguous unit cells.

The local constitutive relation between the strain-rate $\dot{\varepsilon}_{ij}(\mathbf{x})$ and the deviatoric stress $\sigma'(\mathbf{x})$ is given by the classic incompressible rate-dependent crystal plasticity equation:

$$\dot{\varepsilon}_{ij}(\mathbf{x}) = \sum_{s=1}^{N_s} m_{ij}^s(\mathbf{x})\dot{\gamma}^s(\mathbf{x}) = \dot{\gamma}_0 \sum_{s=1}^{N_s} m_{ij}^s(\mathbf{x}) \left(\frac{m^s(\mathbf{x}) : \sigma'(\mathbf{x})}{\tau^s(\mathbf{x})}\right)^n \operatorname{sgn}(m^s(\mathbf{x}) : \sigma'(\mathbf{x})) \tag{1}$$

where the sum runs over all N_s slip systems, and where $m^s(\mathbf{x}) = \frac{1}{2}(n^s(\mathbf{x}) \otimes b^s(\mathbf{x}) + b^s(\mathbf{x}) \otimes n^s(\mathbf{x}))$ is the symmetric Schmid tensor (with $n^s(\mathbf{x})$ and $b^s(\mathbf{x})$ being the normal and Burgers vectors of slip system s), $\dot{\gamma}^s(\mathbf{x})$ and $\tau^s(\mathbf{x})$ are, respectively, the shear-rate and the critical resolved shear stress of

slip system s, $\dot{\gamma}_0$ is a normalization factor, and n the rate-sensitivity exponent. The symbol ":" indicates double contraction of indices. For later use, the rotation-rate of the crystallographic lattice associated with a material point x is given by

$$-\dot{\omega}^p_{ij}(\mathbf{x}) = -\sum_{s=1}^{N_s} \alpha^s_{ij}(\mathbf{x})\dot{\gamma}^s(\mathbf{x}) \tag{2}$$

where $\alpha^s(\mathbf{x}) = \frac{1}{2}(n^s(\mathbf{x}) \otimes b^s(\mathbf{x}) - b^s(\mathbf{x}) \otimes n^s(\mathbf{x}))$ is the anti-symmetric Schmid tensor. If $p(\mathbf{x})$ represents the hydrostatic pressure field, the Cauchy stress field can be written as

$$\sigma_{ij}(\mathbf{x}) = L^0_{ijkl}\dot{\varepsilon}_{kl}(\mathbf{x}) + \varphi_{ij}(\mathbf{x}) - p(\mathbf{x})\delta_{ij} \tag{3}$$

with the polarization field $\varphi_{ij}(\mathbf{x})$ given by

$$\varphi_{ij}(\mathbf{x}) = \sigma'_{ij}(\mathbf{x}) - L^0_{ijkl}\dot{\varepsilon}_{kl}(\mathbf{x}) \tag{4}$$

and with L^0 being the stiffness of a linear reference medium. The choice of L^0 can be quite arbitrary, but the speed of convergence of the method will depend on this choice. In our calculations we used a "Taylor" guess for L^0, i.e. the average over $\{\mathbf{x^d}\}$ of the local linearized secant moduli, obtained by assuming $\dot{\varepsilon}_{ij}(\mathbf{x^d}) = \dot{E}_{ij}$ in Eq. (1).

Combining Eq. (3) with the equilibrium ($\sigma_{ij,j}(\mathbf{x}) = 0$) and the incompressibility conditions:

$$\begin{aligned} &L^0_{ijkl}v_{k,lj}(\mathbf{x}) + \varphi_{ij,j}(\mathbf{x}) - p_{,i}(\mathbf{x}) = 0 \\ &v_{k,k}(\mathbf{x}) = 0 \end{aligned} \tag{5}$$

The system of differential equation (5), with periodic boundary conditions across the unit cell boundary, can be solved by means of the Green function method. An auxiliary system can be written, replacing the polarization term by an unitary body-force term localized in one point, given by the product of Kronecker delta and Dirac delta functions:

$$\begin{aligned} &L^0_{ijkl}G_{km,lj}(\mathbf{x}-\mathbf{x}') + \delta_{im}\delta(\mathbf{x}-\mathbf{x}') - H_{m,i}(\mathbf{x}-\mathbf{x}') = 0 \\ &G_{km,k}(\mathbf{x}-\mathbf{x}') = 0 \end{aligned} \tag{6}$$

In Eq. (6), G_{km} and H_m are the periodic Green functions associated with the velocity and hydrostatic pressure fields. If the Green functions are known, the solutions of the original system of differential equations can be obtained as convolution integrals between such Green functions and the actual polarization term. In the case of the velocity field, after some manipulation:

$$\tilde{v}_k(\mathbf{x}) = \int_{R^3} G_{ki,j}(\mathbf{x}-\mathbf{x}')\varphi_{ij}(\mathbf{x}')\mathrm{d}\mathbf{x}' \tag{7}$$

and its gradient is given by

$$\tilde{v}_{i,j}(\mathbf{x}) = \int_{R^3} G_{ik,jl}(\mathbf{x}-\mathbf{x}')\varphi_{kl}(\mathbf{x}')\mathrm{d}\mathbf{x}' \tag{8}$$

Convolution integrals in direct space are simply products in Fourier space:

$$\hat{\tilde{v}}_k(\boldsymbol{\xi}) = (-\mathrm{i}\xi_j)\widehat{G}_{ki}(\boldsymbol{\xi})\hat{\varphi}_{ij}(\boldsymbol{\xi}) \tag{9}$$

$$\hat{\tilde{v}}_{i,j}(\boldsymbol{\xi}) = \widehat{\Gamma}_{ijkl}(\boldsymbol{\xi})\hat{\varphi}_{kl}(\boldsymbol{\xi}) \tag{10}$$

where the symbol "^" indicates a Fourier transform. The Green operator in Eq. (10) is defined as $\Gamma_{ijkl} = G_{ik,jl}$. The tensors $\widehat{G}_{ij}(\boldsymbol{\xi})$ and $\widehat{\Gamma}_{ijkl}(\boldsymbol{\xi})$ can be calculated by taking the Fourier transform of system (6):

$$\begin{aligned} &\xi_l\xi_j L^0_{ijkl}\widehat{G}_{km}(\boldsymbol{\xi}) - \mathrm{i}\xi_i\widehat{H}_m(\boldsymbol{\xi}) = \delta_{im} \\ &\xi_k\widehat{G}_{km}(\boldsymbol{\xi}) = 0 \end{aligned} \tag{11}$$

Defining (in Fourier space) the (3×3) matrix A' as: $A'_{ik} = \xi_l\xi_j L^0_{ijkl}$, and the (4×4) matrix A'' as

$$A'' = \begin{vmatrix} A'_{11} & A'_{12} & A'_{13} & \xi_1 \\ A'_{21} & A'_{22} & A'_{23} & \xi_2 \\ A'_{31} & A'_{32} & A'_{33} & \xi_3 \\ \xi_1 & \xi_2 & \xi_3 & 0 \end{vmatrix} \tag{12}$$

we obtain, from Eq. (11): $\widehat{G}_{ij}(\boldsymbol{\xi}) = A''^{-1}_{ij}$ $(i,j=1,3)$ and $\widehat{\Gamma}_{ijkl}(\boldsymbol{\xi}) = -\xi_j\xi_l\widehat{G}_{ik}(\boldsymbol{\xi})$.Assigning initial guess values to the strain-rate field in the regular grid $\{\mathbf{x^d}\}$ (e.g. $\tilde{\dot{\varepsilon}}^0_{ij}(\mathbf{x^d}) = 0 \Rightarrow \dot{\varepsilon}^0_{ij}(\mathbf{x^d}) = \dot{E}_{ij}$), and computing the corresponding stress field $\sigma'^0_{ij}(\mathbf{x^d})$ from the local constitutive relation (1) (which requires knowing the initial values of the critical stresses $\tau^s_0(\mathbf{x^d})$, and the Schmid tensors $m^s_{ij}(\mathbf{x^d})$, e.g. from the OIM orientation map, if the pixels of the image coincide with the Fourier grid), allows us to obtain an initial guess for the polarization field in direct space $\varphi^0_{ij}(\mathbf{x^d})$ (Eq. (4)), which in turn can be Fourier-transformed to obtain $\hat{\varphi}^0_{ij}(\boldsymbol{\xi^d})$. Furthermore, assuming that $\lambda^0_{ij}(\mathbf{x^d}) = \sigma^0_{ij}(\mathbf{x^d})$ is the initial guess for a field of Lagrange multipliers associated with the compatibility constraints, the iterative procedure based on augmented Lagrangians proposed by Michel et al. [31] reads as follows. With the polarization field after iteration n being known, the $(n+1)$th iteration starts by computing the new guess for the kinematically admissible strain-rate deviation field:

$$\hat{\tilde{d}}^{n+1}_{ij}(\boldsymbol{\xi^d}) = -\widehat{\Gamma}^{\mathrm{sym}}_{ijkl}(\boldsymbol{\xi^d})\hat{\varphi}^n_{kl}(\boldsymbol{\xi^d}) \quad \forall\boldsymbol{\xi^d} \neq 0 \text{ and } \hat{\tilde{d}}^{n+1}_{ij}(\mathbf{0}) = 0 \tag{13}$$

where $\widehat{\Gamma}^{\mathrm{sym}}_{ijkl}$ is the Green operator, appropriately symmetrized. The corresponding field in real space is thus obtained by application of the inverse FFT, i.e.

$$\tilde{d}^{n+1}_{ij}(\mathbf{x^d}) = \mathrm{fft}^{-1}\{\hat{\tilde{d}}^{n+1}_{ij}(\boldsymbol{\xi^d})\} \tag{14}$$

and the new guess for the deviatoric stress field is calculated from (omitting subindices) [31]:

$$\begin{aligned} \sigma'^{n+1}(\mathbf{x^d}) + L^0 : \dot{\gamma}_0 \sum_{s=1}^{N_s} m^s(\mathbf{x^d})\left(\frac{m^s(\mathbf{x^d}) : \sigma'^{n+1}(\mathbf{x^d})}{\tau^s(\mathbf{x^d})}\right)^n \\ = \lambda^n(\mathbf{x^d}) + L^0 : (\dot{E} + \tilde{d}^{n+1}(\mathbf{x^d})) \end{aligned} \tag{15}$$

The iteration is completed with the calculation of the new guess of the Lagrange multiplier field:

$$\lambda^{n+1}(\mathbf{x^d}) = \lambda^n(\mathbf{x^d}) + L^0 : (\tilde{\dot{\varepsilon}}^{n+1}(\mathbf{x^d}) - \tilde{d}^{n+1}(\mathbf{x^d})) \tag{16}$$

Expressions (15) and (16) guarantee the convergence of: $\dot{\varepsilon}(\mathbf{x^d})$ (i.e. the strain-rate field related with the stress through the constitutive equation) towards $d(\mathbf{x^d})$ (i.e. the

kinematically admissible strain-rate field) to fulfill compatibility, and the Lagrange multiplier field $\lambda(\mathbf{x^d})$ towards the stress field $\sigma'(\mathbf{x^d})$ to fulfill equilibrium.

Upon convergence, the predicted overall and local mechanical response is advanced, and the microstructure is updated using an explicit scheme, as follows. At time t, the effective stress is calculated averaging the local stress field. The calculated strain-rate field is assumed to be constant during a time interval $[t, t+\Delta t]$. The macroscopic and local strain increments are then calculated as: $\Delta E_{ij} = \dot{E}_{ij} \times \Delta t$ and $\Delta\varepsilon_{ij}(\mathbf{x^d}) = \dot{\varepsilon}_{ij}(\mathbf{x^d}) \times \Delta t$. The local crystallographic orientations are updated according to the following local lattice rotation:

$$\omega_{ij}(\mathbf{x^d}) = (\dot{\Omega}_{ij}(\mathbf{x^d}) + \tilde{\dot{\omega}}_{ij}(\mathbf{x^d}) - \dot{\omega}^p_{ij}(\mathbf{x^d})) \times \Delta t \tag{17}$$

where $-\dot{\omega}^p_{ij}(\mathbf{x^d})$ is given by Eq. (2), and $\tilde{\dot{\omega}}(\mathbf{x^d})$ is obtained by back-transforming the converged antisymmetric field:

$$\hat{\tilde{\dot{\omega}}}_{ij}(\boldsymbol{\xi}^{\mathbf{d}}) = -\widehat{\Gamma}^{\text{antisym}}_{ijkl}(\boldsymbol{\xi}^{\mathbf{d}})\hat{\dot{\rho}}_{kl}(\boldsymbol{\xi}^{\mathbf{d}}) \quad \forall \boldsymbol{\xi}^{\mathbf{d}} \neq 0 \text{ and } \hat{\tilde{\dot{\omega}}}_{ij}(\mathbf{0}) = 0 \tag{18}$$

The critical resolved shear stresses of the deformation systems associated with each material point should also be updated, due to strain hardening, after each deformation increment. While any arbitrary hardening law may be implemented, we used here an extended Voce law [38], characterized by an evolution of the critical stress with accumulated shear strain of the form:

$$\tau^{s*}(\mathbf{x^d}) = \tau^s_{\text{i}} + (\tau^s_{\text{f}} + \theta^s_{\text{f}} \times \Lambda(\mathbf{x^d}))[1 - \exp(-\Lambda(\mathbf{x^d}) \times |\theta^s_{\text{i}}/\tau^s_{\text{f}}|)] \tag{19}$$

where $\Lambda(\mathbf{x^d})$ is the total accumulated shear strain in the material point, given by

$$\Lambda(\mathbf{x^d}) = \sum_{t=1}^{N_t} \sum_{s=1}^{N_s} \dot{\gamma}^s(\mathbf{x^d}, t) \times \Delta t \tag{20}$$

where N_t is the number of time increments, and τ^s_{i}, τ^s_{f}, θ^s_{i} and θ^s_{f} are the initial critical stress, the initial hardening rate, the asymptotic hardening rate and the back-extrapolated critical stress, respectively. In addition, we consider a coupling hardening matrix $h^{ss'}$, which empirically accounts for the obstacles that slip on system s' represent for the propagation of dislocations on system s. The increase in the critical stress is then calculated as

$$\Delta\tau^s(\mathbf{x^d}) = \frac{\mathrm{d}\tau^{s*}(\mathbf{x^d})}{\mathrm{d}\Lambda(\mathbf{x^d})} \sum_{s'=1}^{N_s} h^{ss'}\dot{\gamma}^{s'}(\mathbf{x^d}) \times \Delta t \tag{21}$$

After each time increment, the new position of the Fourier points can be determined by calculating the velocity fluctuation term $\tilde{v}_k(\mathbf{x^d})$ back-transforming equation (9), and:

$$X_i(\mathbf{x^d}) = x^d_i + (\dot{E}_{ij}x^d_j + \tilde{v}_i(\mathbf{x^d})) \times \Delta t \tag{22}$$

Evidently, due to the heterogeneity of the medium, the set of convected Fourier points no longer forms a regular grid, after the very first deformation increment. A rigorous way of dealing with this situation was proposed by Lahellec et al. [39] based on the particle-in-cell (PIC) method advanced by Sulsky et al. [40]. The proposed method used two separate grids of points. A regular "computational" grid was used to apply the direct and inverse FFT, as prescribed by the algorithm described above, while a second grid of "material points" (which is not required to be regular, and is usually finer than the computational grid) was used only in real space to account for the constitutive relation. Transfer operators were defined to interpolate between the two grids, when required. In the present case, however, the following simplification was adopted. Neglecting the velocity fluctuation term in Eq. (22), the updated coordinates of the Fourier points can be approximated by

$$X_i(\mathbf{x^d}) \cong x^d_i + \dot{E}_{ij}x^d_j \times \Delta t \tag{23}$$

In this way, the Fourier grid remains regular after each deformation increment. The distances between adjacent Fourier points, however, do change, following the variations of the unit cell dimensions, thus determining an "average stretching" of the grains, following the macroscopic deformation. The rationale for this simplification is that, by inspection of the OIM images (see Fig. 5 below), it becomes evident that for this high-symmetry material at these moderate strains, the actual morphological changes of the constituent grains are not far from the "average stretching", implicit in the simplified expression (23).

4. Unit cell construction

A 2D 256×256 image, containing information on the local (pixel by pixel) crystallographic orientation and a total of 1124 grains, was cropped from the original OIM image, obtained from the free surface of the undeformed Cu sample, consisting originally of 274×339 pixels and 1585 grains. The average grain size (in units of length) of the cropped image, which can be roughly estimated as: $\sqrt{256 \times 256/1124} \times 2\ \mu\text{m} = 7.64 \times 2\ \mu\text{m} = 15.28\ \mu\text{m}$ was very close the original value, given by $\sqrt{339 \times 274/1585} \times 2\ \mu\text{m} = 7.66 \times 2\ \mu\text{m} = 15.32\ \mu\text{m}$.

Since the actual 3D microstructure of the bulk of the sample was not known, a 3D unit cell was built assuming a randomly generated distribution of bulk grains underneath the measured surface grains (i.e. a "3D substrate"), having the same average grain size and overall crystallographic orientation distribution as the surface grains. For this, a 3D Voronoi was generated (note that, since the FFT-based calculation requires a discrete description of the microstructure on a regularly spaced grid, the procedure is simpler than in the case of having to determine the exact position of the boundaries between Voronoi cells in a continuum), as follows: (a) the number of Fourier points in the third dimension (z-direction) was chosen to be 32, resulting in a unit cell of $256 \times 256 \times 32 =$ 2,097,152 Fourier points. Note that this choice gives, in average, about four grains along the third dimension. (b) The number of grains of the Voronoi structure was calcu-

lated as $2{,}097{,}152/(7.64)^3 = 4703$. (c) Then, 4703 points were randomly distributed in a 3D unit cell. This Poisson distribution of points constitutes the nuclei of the random grains. (d) The sides of the unit cell were divided into equispaced $256 \times 256 \times 32$ Fourier points, or voxels. Each Fourier point was assigned to its nearest nucleus (accounting for periodic boundary conditions across the unit cell limits), determining 4703 different domains (grains).

Next, the measured 2D and the numerically generated 3D microstructures were merged as follows. First, every 3D grain having a voxel on the first z-layer was removed, and every voxel corresponding to these removed grains was assigned with the crystallographic orientation of the pixel of the 2D OIM image having the same x- and y-coordinates. These replacements determined a structure of "extruded" (columnar) grains of variable depth in the z-direction (from one to several layers), with its first ("surface") layer having the same topology as the OIM image, lying on a 3D substrate. The number of grains of this intermediate configuration decreased to 3965 grains. Subsequently, in order to obtain more realistic grain shapes, especially in the transition zone between the columnar grains and the 3D substrate, the microstructure was "annealed" using a standard 3D Monte Carlo (MC) grain growth model with isotropic boundary properties (see e.g. Ref. [41] for details). The grain's identification numbers at each grid point were used directly in the MC model as spin numbers and no modification of the grid was necessary or used. The voxels in the surface layer that corresponded to the measured OIM scan (reproduced on the bottom layer, with periodic boundary conditions) were fixed and not allowed to evolve. All other parts of the microstructure were allowed to evolve, with the result that grain boundaries moved to minimize their areas. The annealing was run for 1,000,000 MC steps, at which time evolution had essentially ceased because of the pinning effect of the surface layers. The number of grains was further decreased to 3697 in the final annealed microstructure.

As already pointed out, after carrying out this numerical treatment of the unit cell's microstructure, the first layer of the resulting representative volume element turned out to have the exact same topology as the OIM image. However, without any further manipulation of this configuration, the measured "surface" grains would become bulk grains, upon the imposition of periodic boundary conditions across the unit cell. Therefore, in order to reproduce the actual free surface condition on the measured grains, the bottom five z-layers (z-layers 28–32) of Fourier points were replaced by a "buffer zone", or "gas phase", with infinite compliance (i.e. identically zero local stress). Such gas phase allowed us to consider the presence of surface grains (corresponding precisely to the grains whose local orientations were actually measured by OIM) while keeping, at the same time, the periodicity across the unit cell (this buffer "disconnects" the surface from the bottom of the periodic repetition of the unit cell, located immediately above). A similar technique was used in phase field simulations of microstructural evolution in thin films [42]. The resulting configuration of the 3D unit cell, including the zero-stress buffer zone, is shown schematically in Fig. 3. In the next section, we show and compare results of both unit cell configurations, i.e. the original one resulting from the merging of the OIM and Voronoi structures plus the MC annealing, with no buffer zone (equivalent to neglecting the surface character of the grains whose orientations were measured by OIM), and the one including the gas phase, for a direct comparison with the OIM measurements.

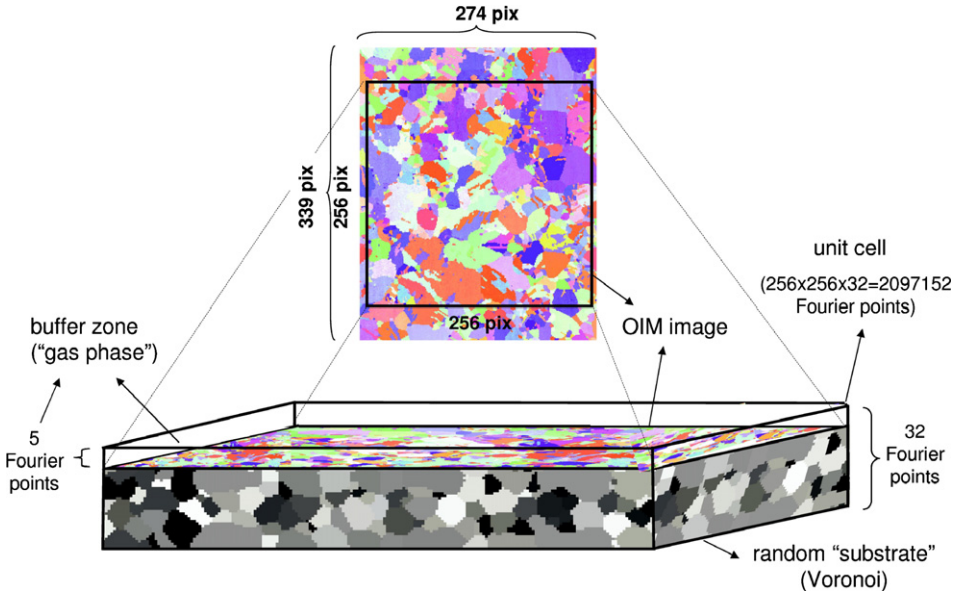

Fig. 3. Schematic representation of the 3D unit cell used in the FFT-based simulations of local orientation and misorientation evolution, with direct input from OIM images.

Besides the evident limitation of the procedure followed to construct the 3D unit cell (i.e. the lack of experimental information forced us to guess the 3D microstructure beneath the OIM image), other possible sources of inaccuracies should be acknowledged. On the one hand, unlike the Voronoi microstructure (in which periodic boundary conditions were imposed through the unit cell boundaries during its generation), the OIM image exhibits abrupt changes (from grains located inside the unit cell to other, completely uncorrelated grains located across the unit cell limits) when periodic boundary conditions are imposed. This could adversely affect the model predictions, especially for grains close to the unit cell boundaries. However, the inaccuracies associated with the presence of these spurious "grain boundaries" appear to be of minor importance (see Ref. [35] for a detailed discussion). On the other hand, the procedure described above does not take into account the fact that grains with large 2D areas are more likely to go deeper into the third dimension.

5. Results and discussion

FFT-based simulations of the tensile deformation of the polycrystalline Cu sample were performed using the two above-described unit cells (with and without the buffer zone). The rate-sensitive crystal plasticity equation (1) was used as the local constitutive relation, assuming glide on the 12 $(1\,1\,1)\langle 1\,1\,0\rangle$ systems as the active slip mode, and a viscoplastic exponent $n = 20$. The initial distribution of critical resolved shear stresses was assumed to be uniform. The extended Voce law hardening parameters (see Eq. (19)), adjusted to match the experimental macroscopic stress–strain curve measured during the tensile deformation of the Cu sample, were: $\tau_i^s = 11$ MPa, $\tau_f^s = 15.5$ MPa, $\theta_i^s = 430$ MPa and $\theta_f^s = 110$ MPa, $(s = 1,12)$ and $h^{ss'} = 1$, for all ss'. The experimental and simulated stress–strain curves are shown in Fig. 4.

Fig. 5 shows the inverse pole figures of the initial and final OIM global textures and the corresponding prediction using the FFT-based approach. The initial texture already exhibits maxima near $\langle 0\,0\,1\rangle$ and $\langle 1\,1\,1\rangle$ (related to the previous thermomechanical history of the material). The measured and predicted textures after 11% tension show similar trends. The maxima near $\langle 0\,0\,1\rangle$ and $\langle 1\,1\,1\rangle$ are stable, and the region near $\langle 1\,1\,0\rangle$ is depleted of orientations. The matching between the measured and predicted locations of the 0.5 and 1 mrd (multiples of random distribution) lines is remarkable. The comparison between the 2 and 3 mrd lines reflects some minor quantitative differences between the experimental and predicted textures.

Fig. 6a shows the registered initial and 11% strain OIM images (the latter is shown already cropped), measured on the surface of the Cu sample. The post-deformation image clearly indicates the development of intragranular misorientations, in terms of noticeable color grades inside several grains. The location and number of pixels of the 13 largest ("marked") grains are shown in Fig. 6b. The initial orientations of the marked grains can be seen in Fig. 7, in an inverse pole figure representation. Fig. 7 also shows the trajectories of the mean orientations of these marked grains (except for grain #5, which is very close and behaves very similarly to grain #6, and was not plotted for sake of clarity), as predicted by the FFT-based model (with buffer zone). The small crosses defining these trajectories were obtained in increments of 1% overall plastic strain. The actual final average orientations, measured with OIM, are shown as well. In the region close to the $\langle 0\,0\,1\rangle$ corner, grains #1, #9 and #12 rotate towards the stable orientation

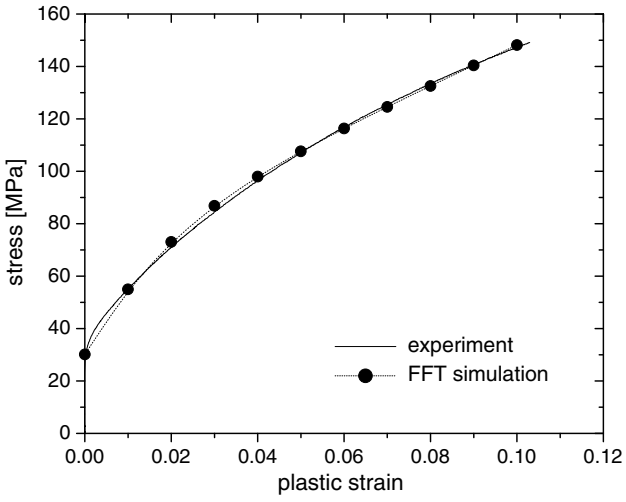

Fig. 4. Experimental and simulated stress–strain curves of the Cu sample deformed 11% in tension.

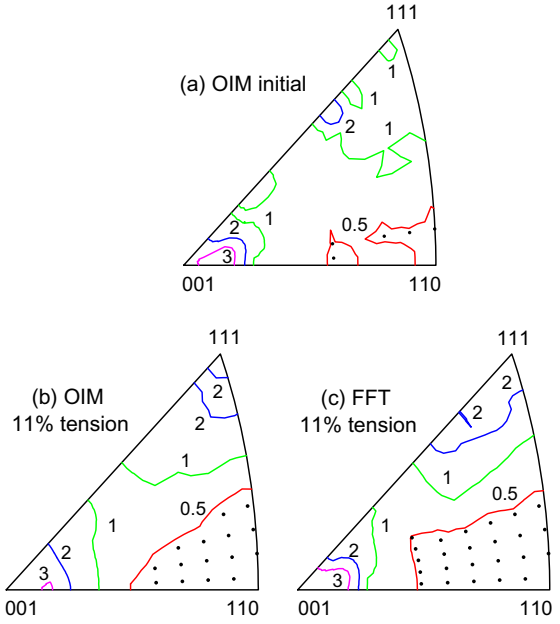

Fig. 5. Inverse pole figures corresponding to global textures at the surface of the Cu sample: (a) initial texture, measured with OIM; (b) texture after 11% tension, measured with OIM; (c) texture after 11% tension, predicted with the FFT-based approach. Lines: multiples of random distributions (mrd). Dots: orientation regions below 0.5 mrd

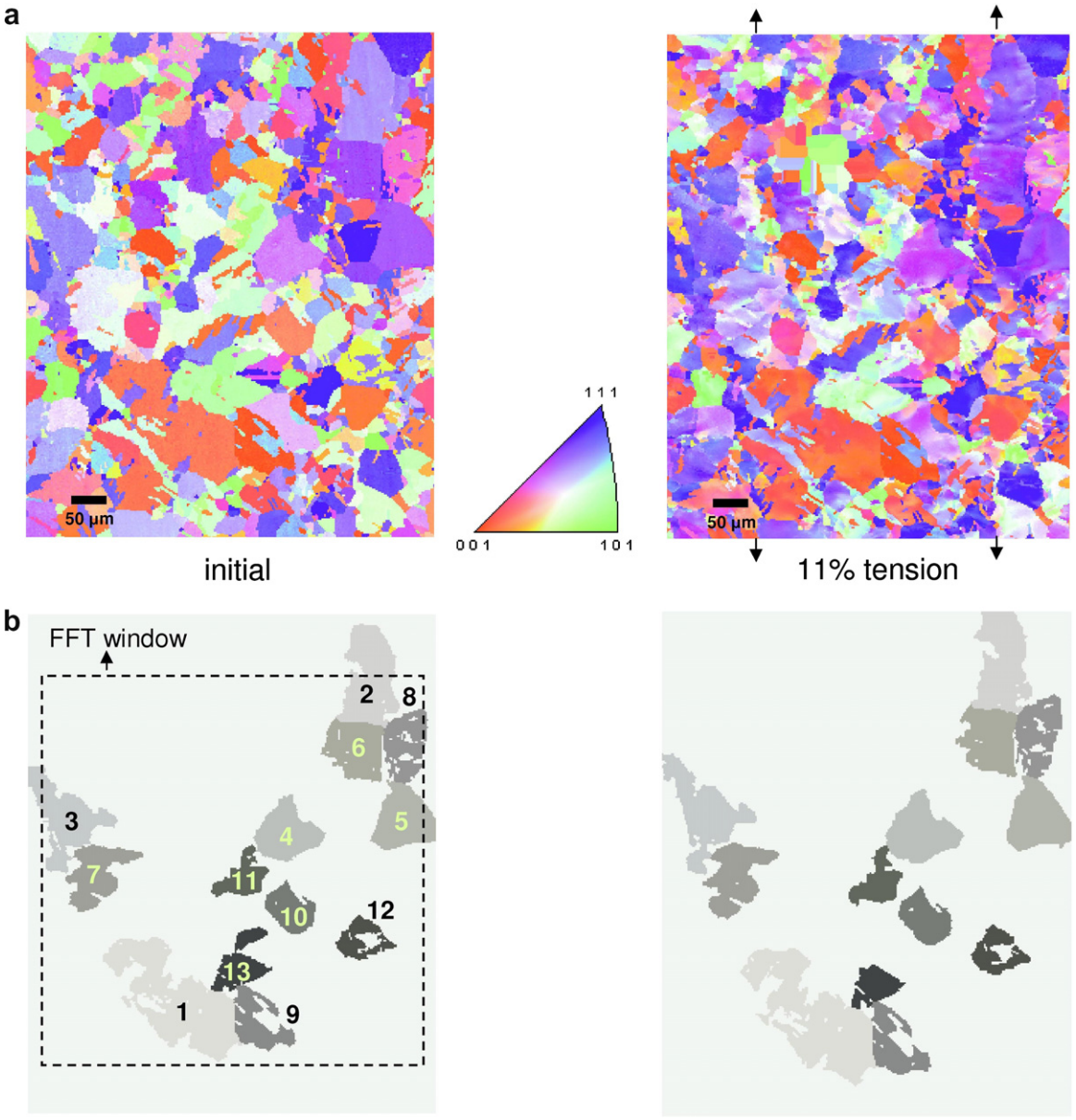

Fig. 6. (a) Registered OIM images of the Cu polycrystal before deformation and after 11% tensile strain. (b) Location and morphology of the 13 largest grains, before and after deformation. The "FFT window" shows the 256 × 256 pixel region that was actually used to construct the unit cell.

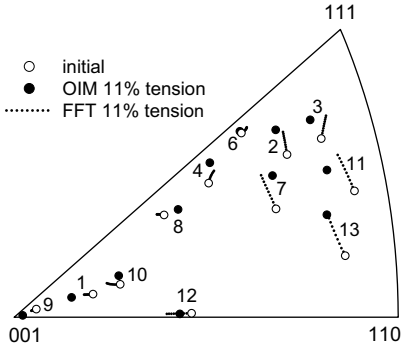

Fig. 7. Inverse pole figure of the measured initial orientation and the final average orientation of the largest grains, and trajectories predicted with the FFT-based approach.

⟨001⟩, a trend that is predicted, at least qualitatively, by the model. Grains with initial orientations close to the upper half of the ⟨001⟩–⟨111⟩ line (#4, #5 and #6) exhibit rotations along this line towards the other stable orientation, i.e. ⟨111⟩ (also well reproduced by the model). The grains starting near the ⟨110⟩ corner (#11 and #13), or in intermediate orientations between ⟨110⟩ and the mid-section of the ⟨001⟩–⟨111⟩ line (#2, #3 and #7) rotate towards this line, presumably on their way towards the stable orientation ⟨111⟩. The total rotations of these grains are the largest. All these features are acceptably reproduced by our simulations, except for the reorientation of grain #3, which is predicted to be directly towards ⟨111⟩. Finally, the trends of grain #10, and especially grain #8 (which starts close a well-known transition point on the

⟨001⟩–⟨111⟩ line, close to ⟨113⟩ [43–46]), are not adequately reproduced by the model. It is also interesting to compare (while keeping in mind the obvious differences, i.e. Cu vs. Al, 2D vs. 3D) the above trends and the 3DXRD characterization done by Winther et al. [24] of the rotations of bulk grains of an Al polycrystal deformed in tension. The rotations measured on Cu surface grains (and well predicted by our model) with initial orientations belonging to three of the four "regions" characterized in [24] (i.e. region 1: close to ⟨111⟩, region 2: near the upper half of the ⟨110⟩–⟨111⟩ line, and region 4: near the ⟨100⟩ corner) are also in acceptable agreement with the observations of Winther et al. No grains with orientations in Winther et al.'s region 3 (close to ⟨221⟩) were large enough in the Cu sample to be used for this analysis.

Although interesting, the above-described reasonable agreement between the measured and predicted average orientation evolution is not surprising, since almost every (either full-field or mean-field) model based on crystal plasticity qualitatively predicts the development of two stable texture components in ⟨001⟩ and ⟨111⟩ in fcc materials deformed under tension (e.g. see comparisons of Winther et al.'s measurements with corresponding Taylor and self-consistent predictions [24]). A much less investigated aspect of the local texture evolution of these materials is reported in Table 1, which shows the comparison between the measured and the predicted values of average misorientations (in degrees) inside the marked grains. Together with the size (in pixels) of the grains, two predicted values are reported for each grain: the fourth column shows the predictions obtained using the unit cell shown in Fig. 3, i.e. including the buffer zone, and therefore considering the effect of measuring misorientations in surface grains. The fifth column displays the predictions obtained for a unit cell without the buffer zone, giving an idea of the misorientation values that would be measured if the grains were bulk grains. Evidently, the proper consideration in the model of the surface character of the grains whose average misorientations were measured by OIM leads to a good agreement with the corresponding experimental values. On the other hand, the artificial assumption of the bulk character of these grains tends to underestimate (by factors in the range [0.71, 0.97], with an average of about 0.8, for the set of largest grains) the actual average misorientations of surface grains. The reason why the predictions obtained under the bulk assumption fall short is related to this being a more constrained configuration, compared with the actual boundary conditions imposed on the surface grains.

The very good agreement between experiments and simulations (using the adequate unit cell configuration, including the buffer zone) obtained in this grain-by-grain comparison is striking, since the substrate microstructure chosen for the modeling is evidently different from the real one. Indeed, a strong dependence of the neighborhood should be expected since the intragranular fields depend not only on the grain's orientation, but also on the deformation of neighboring crystals (including those in the third dimension), as reported experimentally [47] and numerically [48]. Here, however, only average misorientations of the largest grains were compared, corresponding to grain areas ranging between 10 and 60 times the average over the entire image. These crystals were surrounded by a large number of smaller grains. Consequently, the local neighborhood of these large grains probably had a minor effect on their mechanical response, leading to the good agreement described above. This observation is also consistent with the smaller fluctuations of the average misorientation measured in large grains (as evidenced in Fig. 2) due to the limited influence of their neighbors.

Table 1
Area (in pixels) and average misorientation of the 13 largest grains after 11% tensile strain, measured by OIM and predicted with the FFT-based approach, with and without buffer zone

Grain #	Number of pixels	Average misorientation OIM 11% tension (°)	Average misorientation FFT 11% tension (°)	Average misorientation FFT 11% tension (no buffer) (°)
1	3625	2.89	2.18	1.81
2	2019	2.52	2.05	1.64
3	1842	2.92	2.97	2.25
4	1479	2.86	2.33	2.27
5	1466	2.26	2.35	1.76
6	1380	3.14	2.70	1.91
7	1331	3.37	3.06	2.89
8	1113	3.21	2.62	2.12
9	955	2.65	2.80	2.22
10	830	2.92	2.37	1.81
11	692	2.22	2.79	1.99
12	639	4.33	3.36	2.39
13	596	3.09	3.26	2.83

Another interesting observation is that, except for grain #12, which exhibits the largest average misorientation, the initial orientations of other grains with measured misorientations larger than 3.0° (#6, #7, #8 and #13) lie in a region of the stereographic triangle spanning from ⟨110⟩ towards the midsection (from 1/3 to 2/3) of the ⟨001⟩–⟨111⟩ line. While in the case of grain #12 the high average misorientation seems to be related to its particular morphology (note in Fig. 5b that this grain has a large "hole" in its center, filled by another grain with a completely different orientation, a configuration that may determine a relative "disconnection" between different parts of grain #12), for the rest of the grains, their initial orientations belonging to the above region may be related to their relatively large average misorientation.

To elucidate whether this orientation dependence does exist (and if our model is capable of reproducing it), we investigated the behavior of a larger number of representative grains. Fig. 8a shows a comparison between the average misorientation distribution of the 306 largest grains of the original OIM figure at 11% tension (i.e. same as Fig. 1c) and the FFT-based predictions for the same number of largest grains. Evidently, the shape of the distributions and their mean values, i.e. 2.78° (OIM) vs. 3.09° (FFT) are comparable. However, the above comparison does

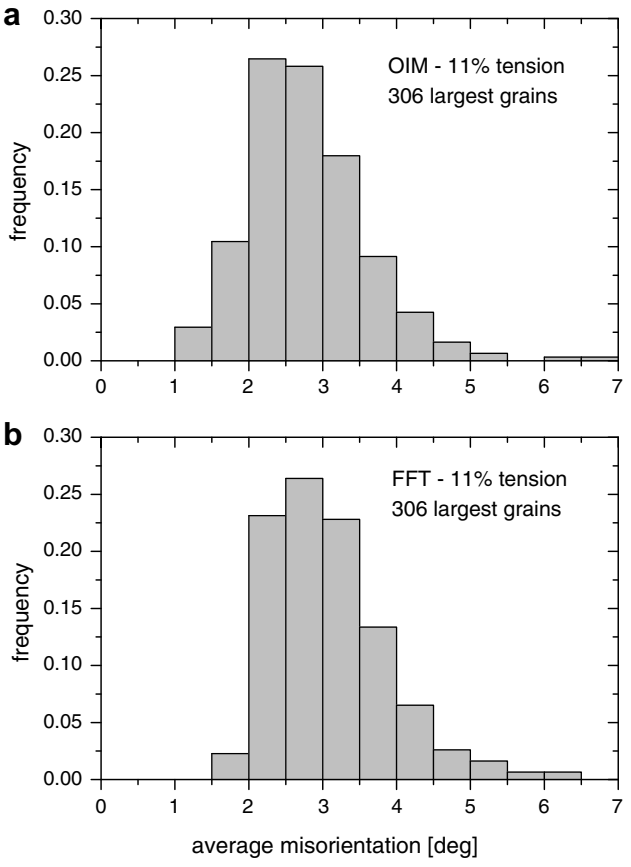

Fig. 8. Distribution of average intragranular misorientations of the 306 largest grains after 11% tensile deformation: (a) extracted from the scanned area of the deformed Cu sample, and (b) as predicted by the FFT-based model.

not reveal any orientation dependence, since misorientations of grains of all orientations were counted to build those distributions.

In order to visualize the orientation dependence of the average misorientations, Fig. 9 shows the average orientations (given by each pole projected in the inverse pole figure) and the average misorientations (given by the different symbols used) of the largest 306 grains, as measured by OIM and predicted with the FFT-based approach, after 11% tensile strain. The misorientation values of the grains were grouped into six bins of equal size, and different symbols were assigned to each bin. The first observation is that, as expected, after 11% tension there is already a mild but noticeable trend of large grains to rotate towards one of the stable ⟨0 0 1⟩ and ⟨1 1 1⟩ orientations (the region near ⟨1 1 0⟩ is mildly depleted of orientations). Moreover, it is evident (from both the experiments and the simulations) that most of the grains with the highest average misorientation are grains transitioning from their initial orientation near ⟨1 1 0⟩ towards the stable orientations. This observation can be explained in the following terms: depending on their initial orientation, the grains of an fcc polycrystal in tension are attracted towards one of the two stable orientations, i.e. ⟨0 0 1⟩ or ⟨1 1 1⟩ (the latter, directly or via the ⟨0 0 1⟩–⟨1 1 1⟩ line). Grains with orientations in a region of the orientation space, spanning from near ⟨1 1 0⟩ towards the midsection of the ⟨0 0 1⟩–⟨1 1 1⟩ line, can be pulled simultaneously towards both stable orientations. In this case, the interaction with neighbor grains may define the preference of different portions of these "indecisive" grains to rotate towards different stable orientations. This conflicting attraction towards two completely different orientations may be accommodated by the development of relative higher misorientations between different subdomains of a grain. This corresponds to the transition band concept documented by Dillamore et al. [44,45].

Finally, in order to determine the ability of the present FFT-based model to capture the grain size effect on the average misorientation, Fig. 10 shows the ratio between the measured and the predicted average misorientations of the 57 largest grains, as function of their grain area size (in pixels). This plot suggests that the model tends to slightly underestimate the average misorientation of large

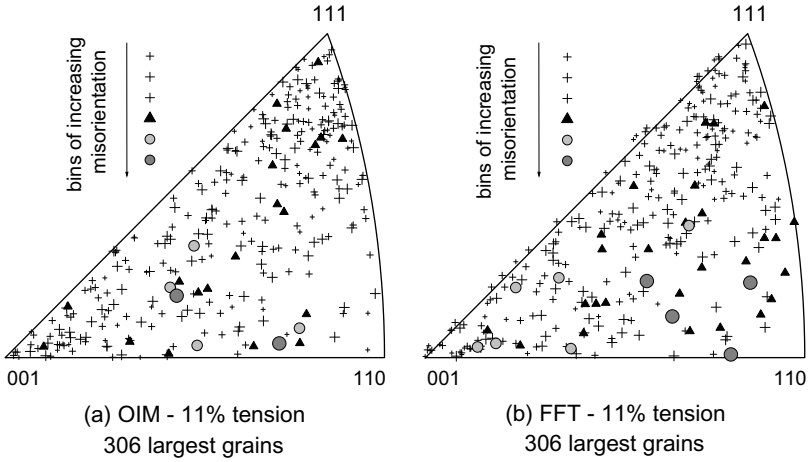

Fig. 9. Inverse pole figures of the average orientations and misorientations of the 306 largest grains after 11% tensile strain: (a) measured by OIM, and (b) predicted with the FFT-based approach. The misorientations were grouped in bins of equal size, and different symbols were assigned to each bin.

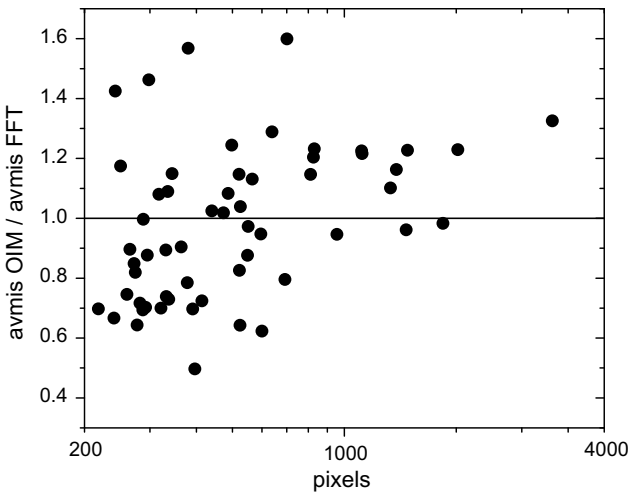

Fig. 10. Ratio between measured and predicted average misorientations of the 57 largest grains, as a function of grain size (in pixels).

grains. This disagreement could be related with the assumption of uniform initial distribution of critical resolved stresses, which may turn out to be too crude. Under this assumption all grains deformed initially under the same resolved shear stress on the most active slip systems, irrespective of their size. The difference between the apparent grain size (in units of length) between the grains with the largest (3625 pixels) and smallest (218 pixels) areas accounted for in Fig. 9 is: $2\ \mu m \times \sqrt{3625} = 120\ \mu m$ vs. $2\ \mu m \times \sqrt{218} = 29.5\ \mu m$. If we had assumed, by analogy with the Hall–Petch law which gives the yield stress σ_y as a function of grain size d (i.e. $\sigma_y = \sigma_0 + k_{hp} \times d^{1/2}$, where σ_0 and k_{hp} are material-dependent parameters), the following dependence of the initial critical resolved shear stress with the grain size: $\tau_i^s = (\sigma_0 + k_{hp} \times d^{1/2})/M$ (where M is the average Taylor factor), and used typical parameters for Cu, i.e. $\sigma_0 = 25$ MPa and $k_{hp} = 0.14$ MPa $m^{-1/2}$ [49], the critical resolved shear stress of the 218 pixel grain would have been 1.33 times higher than the one of the largest grain (and even higher for smaller grains). Hence, under these assumptions, large grains, being softer, would have carried more deformation than small grains, and consequently the predicted average misorientations would have increased in large grains.

6. Concluding remarks

A FFT-based full-field formulation for viscoplastic polycrystals was applied to the study of the subgrain texture evolution in a Cu aggregate deformed under tension. Direct input was obtained from OIM images, for the construction of the initial unit cell. A methodology to build a three-dimensional unit cell, including the 2D OIM data, a 3D substrate and the presence of a free surface, was given. The average orientations and misorientations of large grains, predicted with the FFT-based approach after 11% tensile strain, were directly compared with OIM measurements. The experimental data and the predictions showed good agreement. The differences of having measured misorientations in surface grains, compared with bulk grains, were estimated. A ratio of about 0.8 between average misorientations developing inside bulk and surface grains was obtained. The orientation dependence of the average misorientations was also studied. Again, measurements and predictions showed reasonable agreement. Grains with initial orientation near $\langle 1\,1\,0\rangle$ tend to develop higher misorientations as deformation proceeds. Attraction towards the two different stable orientations (i.e. corresponding to the alignment of the $\langle 0\,0\,1\rangle$ and the $\langle 1\,1\,1\rangle$ crystal orientations with the tensile axis) of different subdomains inside these grains, influenced by interactions with different neighbors, may be responsible for this behavior. Only full-field models such as the FFT-based formulation, which account for topological information and grain interaction in the determination of the local micromechanical fields, can capture these effects.

Evidently, there is plenty of room for improving the proposed model. Some possible improvements were suggested in the text above, e.g. implementation of a local morphological update scheme, by adapting the particle-in-cell method to polycrystals [39,40], and consideration of a grain size dependence on the initial distribution of critical stresses. Furthermore, not only can this dependence of grain size on the initial critical stresses be introduced in the model, but the grain-size dependence of the strain-hardening behavior can also be considered, via calculation of Nye's tensor of geometrically necessary dislocation (GND) density (e.g. [50]). Since Nye's tensor is defined in terms of the local curvature field (i.e. the orientation-gradient field), it can be easily mapped onto the Fourier grid as a post-processing treatment, after each deformation increment. The resulting GND density field should then be entered in a new hardening law, which, as opposed to the Voce law, must be formulated explicitly in terms of dislocation densities (e.g. [7,13,51,52]). The access to this dislocation density information may be also instrumental in extending the present deformation model to predict recrystallization.

In terms of further validation of the model results, a more refined comparison with OIM data of higher-order moments of the misorientation distribution [20] can be pursued. Also, the simultaneous comparison of model results with orientation data and local deformation data obtained by means of image analysis (e.g. [7,10,16]) or microdiffraction techniques can greatly contribute to further validating the proposed model. In reference to the latter, it is worth mentioning that a scanning Laue experiment has been carried out on the same Cu specimen [53] at the Advanced Light Source's white-beam microdiffraction facility [54]. This technique provides detailed maps of orientation and stress distributions, with micrometric resolution, and can be used as another very valuable means of validation of the present model's predictions.

Finally, another great improvement would be to use experimental 3D orientation data to construct the unit cell

for the FFT-based calculation, and to validate the model results. Since a non-destructive technique is required, the best candidate for this is 3DXRD (e.g. [55]).

Acknowledgments

The authors wish to thank Profs. Pierre Suquet (CNRS Marseille, France) and Deborah Sulsky (University of New Mexico, USA) and Drs. Wolfgang Pantleon and Grethe Winther (Risø National Laboratory, Denmark) for fruitful discussions.

References

[1] Liu Y, Ponte Castañeda P. J Mech Phys Solids 2004;52:467.
[2] Lebensohn RA, Liu Y, Ponte Castañeda P. Acta Mater 2004;52:5347.
[3] Lebensohn RA, Tomé CN, Ponte Castañeda P. Philos Mag 2007;87:4287.
[4] Becker R. Acta Metall Mater 1991;39:1211.
[5] Becker R, Panchanadeeswaran S. Acta Metall Mater 1995;43:2701.
[6] Mika DP, Dawson PR. Mater Sci Eng A 1998;257:62.
[7] Delaire F, Raphanel JL, Rey C. Acta Mater 2001;48:1075.
[8] Barbe F, Decker L, Jeulin D, Cailletaud G. Int J Plasticity 2001;17:513.
[9] Barbe F, Decker L, Jeulin D, Cailletaud G. Int J Plasticity 2001;17:537.
[10] Raabe D, Sachtleber M, Zhao Z, Roters F, Zaefferer S. Acta Mater 2001;49:3433.
[11] Bhattacharyya A, El-Danaf E, Kalidindi SR, Doherty RD. Int J Plasticity 2001;17:861.
[12] Delannay L, Logé RE, Chastel Y, Signorelli JW, Van Houtte P. Adv Eng Mater 2003;5:597.
[13] Cheong KS, Busso EP. Acta Mater 2004;52:5665.
[14] Diard O, Leclercq S, Rousselier G, Cailletaud G. Int J Plasticity 2005;21:691.
[15] Delannay L, Jacques PJ, Kalidindi SR. Int J Plasticity 2006;22:1879.
[16] Musienko A, Tatschl A, Schmidegg K, Kolednik O, Pippan R, Cailletaud G. Acta Mater 2007;55:4121.
[17] Huang X. Scripta Mater 1998;38:1697.
[18] Winther G, Huang X, Godfrey A, Hansen N. Acta Mater 2004;52:4437.
[19] Delannay L, Mishin OV, Juul Jensen D, Van Houtte P. Acta Mater 2001;49:2441.
[20] Pantleon W, He W, Johansson TP, Gundlach C. Mater Sci Eng A 2008;483–484:668.
[21] Thorning, Somers MAJ, Wert JA. Mater Sci Eng A 2005;397:215.
[22] Panchanadeeswaran S, Doherty RD, Becker R. Acta Mater 1996;44:1233.
[23] Poulsen HF, Margulies L, Schmidt S, Winther G. Acta Mater 2003;51:3821.
[24] Winther G, Margulies L, Schmidt S, Poulsen HF. Acta Mater 2004;52:2863.
[25] Morawiec A, Pospiech J. Texture Microstuct 1989;10:211.
[26] Krieger Lassen NC, Juul Jensen D, Conradsen K. Acta Crystallogr A 1994;50:741.
[27] Humbert M, Gey N, Muller J, Esling C. J Appl Cryst 1996;29:662.
[28] Morawiec A. J Appl Cryst 1998;31:818.
[29] Glez JC, Driver J. J Appl Cryst 2001;34:280.
[30] Moulinec H, Suquet P. Comput Method Appl Mech Eng 1998;157:69.
[31] Michel JC, Moulinec H, Suquet P. Comput Model Eng Sci 2000;1:79.
[32] Idiart MI, Moulinec H, Ponte Castaneda P, Suquet P. J Mech Phys Solids 2006;54:1029.
[33] Lebensohn RA. Acta Mater 2001;49:2723.
[34] Lebensohn RA, Liu Y, Ponte Castañeda P. Proc R Soc Lond A 2004;460:1381.
[35] Lebensohn RA, Castelnau O, Brenner R, Gilormini P. Int J Solids Struct 2005;42:5441.
[36] Chen LQ. In: Raabe D, Roters F, Barlat F, Chen LQ, editors. Continuum scale simulations of engineering materials. Wenheim: Wiley; 2004. p. 37.
[37] Wang YU, Jin YMM, Khachaturyan AG. J Appl Phys 2002;92:1351.
[38] Tomé CN, Canova GR, Kocks UF, Christodoulou N, Jonas JJ. Acta Metall 1984;32:1637.
[39] Lahellec N, Michel JC, Moulinec H, Suquet P. In: Miehe C, editor. IUTAM symposium on computational mechanics of solid materials. Dordrecht: Kluwer Academic; 2001. p. 67.
[40] Sulsky D, Zhou SJ, Schreyer HL. Comput Phys Commun 1995;87:236.
[41] Rollett AD, Manohar P. In: Raabe D, Roters F, Barlat F, Chen LQ, editors. Continuum scale simulations of engineering materials. Wenheim: Wiley; 2004. p. 77.
[42] Hu SY, Chen LQ. Acta Mater 2004;52:3069.
[43] Chin GY, Mammel WL, Dolan MT. Trans Met Soc AIME 1967;239:1854.
[44] Dillamore IL, Morris PL, Smith CJE, Hutchinson WB. Proc R Soc Lond A 1972;329:405.
[45] Dillamore IL, Katoh H. Metal Sci J 1974;8:73.
[46] Mecking H. In: Wenk HR, editor. Preferred orientation in deformed metals and rocks: an introduction to modern texture analysis. Orlando, FL: Academic Press; 1985. p. 267.
[47] Man J, Obrtlik K, Blochwitz C, Polak J. Acta Mater 2002;87:1425.
[48] Zeghadi A, N'Guyen F, Forest S, Gourgues AF. Philos Mag 2007;87:1425.
[49] Fu HH, Benson DJ, Meyers MA. Acta Mater 2001;49:2567.
[50] Acharya A, Bassani JL, Beaudoin A. Scripta Mater 2003;48:167.
[51] Tabourot L, Fivel M, Rauch E. Mater Sci Eng A 1997;234–236:639.
[52] Ma A, Roters F, Raabe D. Acta Mater 2006;54:2169.
[53] Castelnau O, Goudeau P, Geandier G, Tamura N, Béchade JL, Bornert M, et al. Mater Sci Forum 2006;524–525:103.
[54] Spolenak R, Brown W, Tamura N, MacDowell A, Celestre R, Padmore H, et al. Phys Rev Lett 2003;90:096102.
[55] Lauridsen EM, Dey SR, Fonda RW, Juul Jensen D. JOM 2006;58:40.